On the nature of intermittency in a turbulent von Kármán flow

H. Faller, D. Geneste, T. Chaabo, A. Cheminet, V. Valori, Y. Ostovan, L. Cappanera, Ch. Cuvier, F. Daviaud, J.-M. Foucaut, et al.

On the nature of intermittency in a turbulent von Kármán flow

H. Faller [1,2]†, D. Geneste [1], T. Chaabo[3], A. Cheminet[3], V. Valori [1], Y. Ostovan[3], L. Cappanera[4], Ch. Cuvier[3] , F. Daviaud [1], J.-M. Foucaut[3], J.-L. Guermond[5], J.-Ph. Laval[3], C. Nore[2], V. Padilla[1], C. Wiertel[1] and B. Dubrulle[1]

[1]Université Paris-Saclay, CEA, CNRS, SPEC, CEA Saclay 91191 Gif sur Yvette cedex, France.

[2]Université Paris-Saclay, CNRS, LIMSI, Laboratoire d'Informatique pour la Mécanique et les Sciences de l'Ingénieur, 91400 Orsay, France

[3]Univ. Lille, CNRS, ONERA, Arts et Metiers Institute of Technology, Centrale Lille, UMR 9014-LMFL-Laboratoire de Mécanique des Fluides de Lille-Kampé de Fériet, F-59000, Lille, France

[4]Department of Mathematics, University of Houston, Houston, TX 77204-3008, USA

[5]Department of Mathematics, Texas A&M University 3368 TAMU, College Station, TX 77843-3368, USA

(Received xx; revised xx; accepted xx)

We have conducted an extensive study of the scaling properties of small scale turbulence using both numerical and experimental data of a flow in the same von Kármán geometry. We have computed the wavelet structure functions, and the structure functions of the vortical part of the flow and of the local energy transfers. We find that the latter obeys a generalized extended scaling, similar to that already observed for the wavelet structure functions. We compute the multi-fractal spectra of all the structure functions and show that they all coincide with each other, providing a local refined hypothesis. We find that both areas of strong vorticity and strong local energy transfer are highly intermittent and are correlated. For most cases, the location of local maximum of energy transfer is shifted with respect to the location of local maximum of vorticity. We however observe a much stronger correlation between vorticity and local energy transfer in the shear layer, that may be an indication of a self-similar quasi-singular structure that may dominate the scaling properties at large order structure functions.

Key words: Turbulent flows, intermittency, universality, von Kármán swirling flows.

1. Introduction

In 1949, Batchelor and Towsend (Batchelor & Townsend 1949) published the first experimental account about inconsistencies in the original turbulence theory of Kolmogorov (Kolmogorov 1941). Measuring various flatnesses of the distribution of velocity derivatives, $\alpha(n) = \overline{\left(\frac{\partial^n u}{\partial x^n}\right)^4} \Big/ \left[\overline{\left(\frac{\partial^n u}{\partial x^n}\right)^2}\right]^2$, they observed an increase of α both with n and with the Reynolds number Re. Their interpretation was that $\partial^n u/\partial x^n$

† Email address for correspondence: hugues.faller@normalesup.org

fluctuates in a manner that is more markedly intermittent as n or Re increases, a fact confirmed by oscillograms of the velocity field derivatives. The finding was summarized in a remarkable concise but visionary paragraph stating that "*energy associated with large wave-number is very unevenly distributed in space. There appear to be isolated regions in which the large wave-numbers are 'activated', separated by regions of comparative quiescence. This spatial inhomogeneity becomes more marked with increase in the order of the velocity derivative, i.e. with increase in the wave-number. It is suggested that the spatial inhomogeneity is produced early in the history of the turbulence by an intrinsic instability, in the way that a vortex sheet quickly rolls up into a number of strong discrete vortices. Thereafter the inhomogeneity is maintained by the action of the energy transfer.*" As noted by Moffatt (2002), such finding describes precisely the now well-admitted intermittency of the vorticity field. In the same time, it provides a clear scenario of building of intermittency and inhomogeneity via first Kelvin-Helmholtz instability (roll up of vorticity sheet), then breaking into discrete blobs of vorticity, and finally action of the energy transfer, that allows to maintain resulting inhomogeneity along scales.

The result of Batchelor and Townsend only concerns intermittency at the dissipative scales. The Kolmogorov (1962) refined theory allows to connect intermittency of the local energy dissipation with (intermittent) correction to scaling of the energy spectrum, or of the velocity structure functions up to the inertial scales. In this picture, there is a direct link between the 'active' regions of intense local dissipation, and the intermittent corrections to scaling. Because the areas of intense dissipation are observed to arise in the vicinity of vorticity filaments (Vincent & Meneguzzi 1994), or sheets (Moisy & Jiménez 2004), there have been several attempts to link intermittency exponents, and vorticity based coherent structures with sometimes conflicting conclusions. By computing wavelet-based velocity and vorticity structure functions, Kestener & Arneodo (2004) found the same intermittency in a 256^3 numerical simulation at $R_\lambda = 140$. However, Nguyen et al. (2019) found a different multifractal spectrum between the two fields in a numerical simulation at the same R_λ but with a large resolution 768^3 (see figures 7-8 of Nguyen et al. (2019)). From the experimental side, Paret & Tabeling (1998) used a simultaneous monitoring of local pressure and velocity in an experimental flow at large Reynolds number to find that the intermittency is decreased when removing from the velocity signal the portions corresponding to very low pressure events (presumably tracing vortex cores). The procedure was improved using wavelet filtering by Chainais et al. (1999), to conclude that the coherent structures do affect the intermittency by acting on the way the cascade develops. Altogether, these results suggest that the vorticity is not the only important ingredient of the intermittency, and that energy transfers should be somehow taken into account, as first argued by Kraichnan (1975).

Indeed, a direct link between intermittent exponent and instantaneous partial local energy transfer at the Kolmogorov scale was found in an experimental turbulent swirling flow using conditional statistics (Debue et al. 2018; Dubrulle 2019). At this time, only velocity measurements on a plane were available, meaning that a fraction of the local energy transfer was missing, and that the vorticity field could not be computed, preventing investigation of possible correlations in between them and with intermittent corrections. Thanks to an outstanding experimental and numerical effort, we now have at our disposal both 3D time and space resolved velocity measurements and numerical data in the same geometry (Cappanera et al. 2020; Debue et al. 2020). The goal of the present paper is thus to gather all results, and investigate how much local energy transfers and vorticity are correlated in between them, and with intermittent corrections to scaling.

2. Definitions

Here, we define the basic tools that we use in our analysis.The time dependence of the velocity field has been removed in the notations for convenience.

2.1. *Vorticity*

The vorticity is a well known object in turbulence. Its magnitude will be mostly used here as

$$\omega = \|\nabla \times \mathbf{u}\|. \tag{2.1}$$

2.2. *Increments and structure functions*

The traditional basic tool to study intermittency is via scaling of the velocity structure functions of order p, defined as:

$$S_p(\ell) = \langle (\delta_{\boldsymbol{\ell}} u)^p \rangle_{\|\boldsymbol{\ell}\|=\ell}. \tag{2.2}$$

Here, $\delta_{\boldsymbol{\ell}} u$ is the longitudinal velocity increment at scale ℓ, defined as

$$\delta_{\boldsymbol{\ell}} u \ = \hat{\boldsymbol{\ell}} \cdot \ (\mathbf{u}(\mathbf{x}+\boldsymbol{\ell}) - \mathbf{u}(\mathbf{x})) \tag{2.3}$$

where $\hat{\boldsymbol{\ell}}$ is the increment direction. Througout the paper, the notation h refers to the local Hölder regularity of $\delta_\ell u$ so that $\delta_\ell u \sim \ell^h$. In Muzy et al. (1991) it was argued that wavelet based velocity increments δW_ℓ may provide more robust results, via the so-called Wavelet Transform Modulus Maxima (WTMM) method. The use of wavelets (Farge 1992; Schneider & Vasilyev 2010) allows to separate strong vorticity structures from the noise. We use a wavelet such that the first moment vanishes. This allows to explore Hölder exponents lower than 1. The velocity increments are defined via the wavelet transform of the tensor $\partial_j u_i$:

$$G_{i,j}(\mathbf{x},\ell) = \int \nabla_j \phi_\ell(\mathbf{r}) u_i(\mathbf{x}+\mathbf{r}) \mathrm{d}\mathbf{r}, \tag{2.4}$$

where $\phi_\ell(x) = \ell^{-3}\phi(x/\ell)$ is a smooth non-negative function with unit integral. From this, we get the wavelet velocity increments as

$$\delta W_\ell(\mathbf{x}) = \ell \max_{i,j} |G_{i,j}(\mathbf{x},\ell)|. \tag{2.5}$$

The interest of such formulation is that it allows to define a velocity increment connected with the scaling properties of the vorticity, by considering the wavelet velocity increment built from the anti-symmetric part of the tensor $\partial_j u_i$, so that:

$$\delta \Omega_\ell(\mathbf{x}) = \frac{\ell}{2} \max_{i,j} |G_{i,j} - G_{j,i}|. \tag{2.6}$$

2.3. *Local energy transfer*

As argued by Kraichnan (1975) and Meneveau (1991), the local energy transfer at scale ℓ may be important to understand the origin of intermittency. For example, consider the local refined hypothesis of Kolmogorov (Kolmogorov (1962)) stating that $(\delta u_\ell)^3 \sim \epsilon_\ell \ell$, where $\sim$ means "has the same statistical properties" and ϵ_ℓ is the energy dissipation over a ball of scale ℓ. It seems more logical in such formula to replace ϵ_ℓ by the local energy transfer at scale ℓ. This is the local refined hypothesis of Kraichnan. The latter can be computed as:

$$\mathscr{D}_\ell^{\mathrm{I}} = \frac{1}{4} \int \nabla \phi_\ell(\boldsymbol{\xi}) \cdot \delta_{\boldsymbol{\xi}} \boldsymbol{u} (\delta_{\boldsymbol{\xi}} \boldsymbol{u})^2 \mathrm{d}\boldsymbol{\xi}, \tag{2.7}$$

where ϕ_ℓ is a smooth non-negative function with unit integral. In the sequel, we choose the same function for computing δW_ℓ, $\delta\Omega_\ell$ and $\mathscr{D}_\ell^{\mathrm{I}}$, and take it as a Gaussian function $\phi_\ell(\mathbf{x}) = \frac{1}{(\ell\sqrt{2\pi})^3}\exp(-\|\mathbf{x}\|^2/2\ell^2)$.

As discussed in Dubrulle (2019), these local energy transfers compete at each scale with the local energy dissipation defined as:

$$\mathscr{D}_\ell^\nu = \frac{\nu}{2}\int \nabla^2\phi_\ell(\boldsymbol{\xi})(\delta_{\boldsymbol{\xi}}\boldsymbol{u})^2 \mathrm{d}\boldsymbol{\xi}. \tag{2.8}$$

The local refined hypothesis of Kraichnan (1975) can then be expressed in a more general fashion following (Dubrulle 1994). Replacing ℓ by $\frac{\langle\delta W_\ell^3\rangle}{\epsilon}$ and ϵ_ℓ by $\langle\mathcal{D}_\ell^{\mathrm{I}}\rangle$ leads to an extended self-similarity as proposed by Dubrulle (2019):

$$\frac{\langle\delta W_\ell^p\rangle}{\langle\delta W_\ell^3\rangle^{p/3}} \propto \frac{\langle|\mathscr{D}_\ell^{\mathrm{I}}|^{p/3}\rangle}{\langle|\mathscr{D}_\ell^{\mathrm{I}}|\rangle^{p/3}}. \tag{2.9}$$

2.4. *Scaling exponents*

The scaling exponents of the velocity structure functions $\zeta(p)$ are defined so that $S_p(\ell) \sim \ \ell^{\zeta(p)}$ in the inertial range. The latter is defined on the range of scales where the Kolmogorov 4/5th law applies, namely:

$$S_3(\ell) = -\frac{4}{5}\epsilon\ell, \tag{2.10}$$

where ϵ is the energy dissipation rate per unit mass. By definition, we thus have $\zeta(3) = 1$. Intermittency corrections are thus encoded by $\tau(p) = \zeta(p) - p/3$, with $\tau(3) = 0$. By extension, we define the scaling exponents of δW_ℓ, $\delta\Omega_\ell$ and $\mathscr{D}_\ell^{\mathrm{I}}$ via the compensated structure functions as

$$\begin{aligned}
\tilde{S}_W(p) &= \frac{\langle\delta W_\ell^p\rangle}{\langle\delta W_\ell^3\rangle^{p/3}} \propto \ell^{\tau_W(p)},\\
\tilde{S}_\Omega(p) &= \frac{\langle\delta\Omega_\ell^p\rangle}{\langle\delta\Omega_\ell^3\rangle^{p/3}} \propto \ell^{\tau_\Omega(p)},\\
\tilde{S}_D(p) &= \frac{\langle|\mathscr{D}_\ell^{\mathrm{I}}|^p\rangle}{\langle|\mathscr{D}_\ell^{\mathrm{I}}|\rangle^p} \propto \ell^{\tau_D(p)},
\end{aligned} \tag{2.11}$$

in the inertial range of scales. Note that in the sequel, we discriminate between the structure functions and their compensated version by a tilde. By definition $\tau_W(3) = \tau_\Omega(3) = \tau_D(1) = 0$. Note that the refined similarity hypothesis given by eq. (2.9) states that $\tau_W(p) = \tau_D(p/3)$.

2.5. *Multi-fractal spectrum*

The multi-fractal spectrum is defined as the Legendre transform of the scaling exponents of the velocity structure functions $\zeta(p)$, so that

$$C(h) = \min_p\left(-ph + \zeta(p)\right). \tag{2.12}$$

Here is adopted the language of large deviations, where $C(h)$ is the rate function of the local scaling exponent. It corresponds to $3 - D(h)$ where $D(h)$ is the dimension of the set of points with local exponent h in the Frisch & Parisi (1985) interpretation. By extension,

we also define the multi-fractal spectra of δW_ℓ, $\delta\Omega_\ell$ and $\mathscr{D}_\ell^{\mathrm{I}}$ as

$$\begin{aligned} C_W(h) &= \min_p \left(-ph + \tau_W(p)\right), \\ C_\Omega(h) &= \min_p \left(-ph + \tau_\Omega(p)\right), \\ C_D(h) &= \min_p \left(-ph + \tau_D(p)\right). \end{aligned} \tag{2.13}$$

Due to properties of the Legendre transform, C_W can be directly compared with $C(h)$ provided a shift:

$$C_W\left(h - \frac{\zeta(3)}{3}\right) = C(h). \tag{2.14}$$

Moreover, if the refined similarity hypothesis (2.9) is satisfied, then $C_W(h) = C_D(3h)$.

3. Description of the von Kármán data sets

The framework of our investigation is turbulence in the von Kármán geometry. The fluid of viscosity ν is confined in a cylinder of radius R =10 cm and height $H = 1.8R$, and set into motion by two counter-rotating impellers, rotating at the same frequency F. It is well known that the von Kármán flow is globally inhomogeneous and anisotropic. Most of the measurements are performed in the center of the tank, where the flow is more homogeneous and isotropic (Ouellette et al. 2006). In the sequel, we use R and $1/2\pi F$ as unit of length and time respectively, so that the global Reynolds number of the flow is $Re = 2\pi R^2 F/\nu$. The properties of the turbulence, such as global dissipation and root-mean-square velocity, depend on the shape of the propeller. In the sequel, we work with the so-called scooping TM87 propeller, described and discussed at length in Debue (2019); Cappanera et al. (2020); Dubrulle (2019). In this case, the flow is fully turbulent for Re $\geqslant$ 6000 and the non-dimensional dissipation per unit mass is $\epsilon = 0.05$ in the turbulent regime. This results in a Kolmogorov length and time of 3 10^{-4}m and 4 10^{-2}s at Re = 6000, which are accessible to both modern particle velocity measurements and direct numerical simulations on a supercomputer. This allows us to combine both numerics and experiments to explore the nature of intermittency in such a turbulent flow.

3.1. *Experimental data sets*

Experimental data were collected with Particle Image Velocimetry (PIV) technics. Hereafter, data named by letters A-E refer to Stereoscopic PIV (SPIV) where the 3 components are deduced by 2D measurements on a plane using 2 cameras (2D-3C). This data set is described in Dubrulle (2019), and corresponds either to global velocity measurement in the whole tank (set A) or data taken in a small window zoomed in the center region of the tank (cases B-E). In each case, either the frequency of the impellers or the viscosity of the fluid were tuned to modify the Reynolds number and the Kolmogorov scale. The corresponding parameters for each case are summarized in table 1. All the SPIV data were acquired at 15 Hz resulting in time uncorrelation between two successive measurements.

Corresponding spatial resolution can be found in table 1. Data named by T-1 to T-4 refer to Tomographic PIV (TPIV) where the 3 components are deduced by tomographic reconstruction (MART method) in a volume using 5 cameras (3D-3C).

This whole data set is acquired at the center of the tank in water by Ostovan et al. (2019) and described in Debue (2019). Velocity fields corresponding to different viscosity or different impeller frequency were measured, as summarized in table 1.

In all experimental cases, time uncorrelation between two measurements is observed. Tomographic reconstruction was done with 5 MART iterations keeping low value of ghost ratio, less than 10%. ϵ and η are computed using global dissipation measured by torque-meters while R_λ is deduced from PIV data. The measurement region and PIV spatial resolution Δx have an impact on the root-mean-square velocity and Taylor microscale defining R_λ, therefore leading to different values of R_λ for given viscosity ν and frequency F. As expressed in table 1, the experiment grid size is rather small, but a very large number of snapshots of the order of 10^4 is available on each dataset. A statistical convergence study for experimental quantities is presented in the appendix of Debue et al. (2018).

3.2. *Numerical data set*

The numerical simulations are performed using the SFEMaNS code (Spectral/Finite Elements code for Maxwell and Navier-Stokes equations). This code uses a hybrid spatial discretization combining spectral and finite elements. In a nutshell the approximation in space is done by using a Fourier decomposition in the azimuthal direction and the continuous Hood-Taylor Lagrange finite element for (r, z) dependencies. The moving counter-rotating impellers are accounted for by using a pseudo-penalty technique. The performance of this technique is discussed in details in section 2.4 of Nore et al. (2018) where shorter impellers are used. Visualizations of turbulent structures, global quantities (such as kinetic energy or fluctuations level) and spatial spectra obtained from hydrodynamical simulations are in agreement with experimental observations (see section 3, Nore et al. (2018)) and thus validate the numerical method.

The rotation frequency is set to $\frac{1}{2\pi}$ and the viscosity is chosen so that the global Reynolds number is $6\ 10^3$. We use 250 complex modes for the Fourier decomposition and the spatial resolution is between $1.3\ 10^{-3}R \simeq \frac{\eta}{3}$ and $4\ 10^{-3}R \simeq \eta$. This unstructured, irregular, mesh is refined in the middle of the tank, where strongest turbulence takes place, with no preferred direction for the mesh. Contrary to the experimental set-up which requires a cooling system, the numerical simulations set the impellers external disks in contact with the top and bottom lids of the tank.

The Reynolds number of the DNS may appear rather low. It was chosen so as to match the lower Reynolds number $\mathrm{Re} = 6\ 10^3$ of the experiments. This choice of Reynolds number was originally made in experiments because $6\ 10^3$ is the lowest Reynolds number at which we know that the flow is fully turbulent, since it is the beginning of the plateau of the dissipation anomaly (see discussion in fig 14 of (Dubrulle 2019)). On the other hand, it is the flow with the largest Kolmogorov scale, enabling to match the highest spatial resolution of our experimental PIV we could achieve. But once more, we stress that it corresponds to a fully turbulent flow. The analysed dataset has 21 uncorrelated snapshots. The high number of grid points $3\ 10^8$ counter-balances a low number of snapshots. A convergence study of computed statistical quantities is presented in the appendix.

4. Comparison between local energy transfer and vorticity

4.1. *Fields*

Figure 1 compares typical instantaneous experimental snapshots of vorticity amplitude with the local energy transfer. This figure corresponds to a slice of an experimental measurement at scale $\ell = 3.2\eta$ in the case T-4, while figure 2 comes from DNS data. As

Case	F (Hz)	Grid Points	Re	R_λ	ϵ(adim)	η(mm)	Δx(mm)	Symbol
A	5	89×65	$3.1\ 10^5$	610	0.045	0.016	2.1	●
B	5	77×79	$3.1\ 10^5$	920	0.045	0.016	0.49	■
C	5	162×157	$3.1\ 10^5$	890	0.045	0.016	0.24	♦
D	1	77×80	$4.1\ 10^4$	300	0.045	0.073	0.49	▲
E	1.2	151×174	$5.8\ 10^3$	72	0.045	0.32	0.24	⋆
T-1	5	$149 \times 103 \times 20$	$3.1\ 10^5$	890	0.045	0.016	0.35	○
T-2	1	$139 \times 101 \times 20$	$6.3\ 10^4$	390	0.045	0.054	0.35	□
T-3	0.5	$148 \times 103 \times 20$	$3.1\ 10^4$	250	0.045	0.09	0.35	◊
T-4	0.1	$149 \times 100 \times 20$	$6.3\ 10^3$	80	0.045	0.3	0.35	△
DNS	$\frac{1}{2\pi}$	$400 \times 800 \times 509$	$6\ 10^3$	72	0.045	0.37	0.1-0.4	—○—

TABLE 1. Parameters describing the main data sets used in this paper. F is the rotation frequency of the impellers in Hz; Re is the Reynolds number based on F and the radius of the tank; R_λ is the Taylor-microscale Reynolds number; ϵ is the global dimensionless energy dissipation; η is the Kolmogorov dissipation length scale; and Δx represents the spatial resolution in the measurements and the DNS. The last column shows the symbols used to represent the experimental data sets. SPIV stands for stereoscopic Particle Image Velocimetry (3 components measurements of the velocity on a plane), while TPIV is Tomographic Particle Image Velocimetry (3 components measurements of the velocity in a cuboid). Since DNS is dimensionless (the cylinder radius is 1), we express Δx and F in terms of the experimental cylinder radius ($R = 10$ cm) and DNS advection time-scale ($T = 1$) for a better comparison.

table 1 shows, these two cases share the same Reynolds number and resolution.

Despite a higher level of noise in the local energy transfer fields, one observes a clear but not exact spatial correlation between location of high vorticity amplitude and high values of $\mathscr{D}_\ell^{\mathrm{I}}$, as already noted in Saw et al. (2016). In figure 2, we show an equivalent comparison between an instantaneous vorticity field and the local energy transfer, in a mid-height plane perpendicular to the rotation axis. Like in the experimental case, we observe a spatial correlation between local maxima of vorticity and local energy transfer, but the correlation is not exact. To quantify further such correlation, we perform in the next section a detailed statistical analysis.

4.2. *Joint statistics*

Figure 3 (resp. 4) shows the joint probability distribution function (PDF) between the amplitude of the vorticity ω and the local energy transfer $\mathscr{D}_\ell^{\mathrm{I}}$ at different scales, in the experiment T-4 (resp. in the DNS). Each PDF is computed over the available data-set which corresponds to the experimental cuboid for the experiment T-4, and to the entire tank excluding the impellers for DNS. Except for very large values of $\omega/\langle\omega\rangle$ and $\mathscr{D}_\ell^{\mathrm{I}}/\epsilon$, all cases display a pyramidal correlation, similar to what was observed in Debue (2019) for the joint PDF between the local dissipation and the local energy transfer $\mathscr{D}_\ell^{\mathrm{I}}$. This is not surprising, since dissipation and enstrophy are known to be correlated. The joint PDF of $\left(\frac{\mathscr{D}_\ell^{\mathrm{I}}}{\epsilon}, \frac{\omega}{\langle\omega\rangle}\right)$ shows that for every scale, strong events of inter-scale transfer are associated with strong vorticity. In the inertial range (see figure 3-b, resp. 4-b) , $\ell \gg \eta$, the PDF is tilted towards positive energy transfers, indicating that the energy is going down the scales. In the viscous range (see figure 3-a, resp. 4-a), the PDF seems to be symmetric with respect to the line $\mathscr{D}_\ell^{\mathrm{I}} = 0$. A marked discrepancy appears between numerical results and experiments when looking at high values of $\omega/\langle\omega\rangle$, since the joint PDF computed from the DNS exhibits a well defined elongated feature, tracing a high degree of correlation

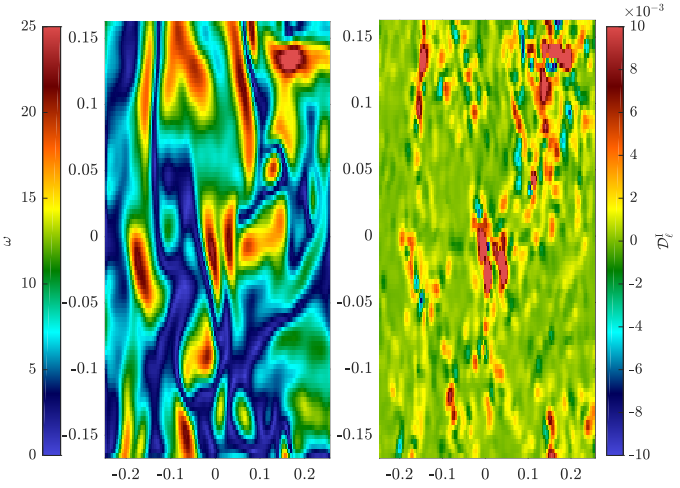

FIGURE 1. Visualization of the vorticity amplitude ω (left panel) and $\mathscr{D}_\ell^{\mathrm{I}}$ (right panel) for $\ell = 3.2\eta$ for the case T-4 of table 1 in a plane containing the cylinder's axis.

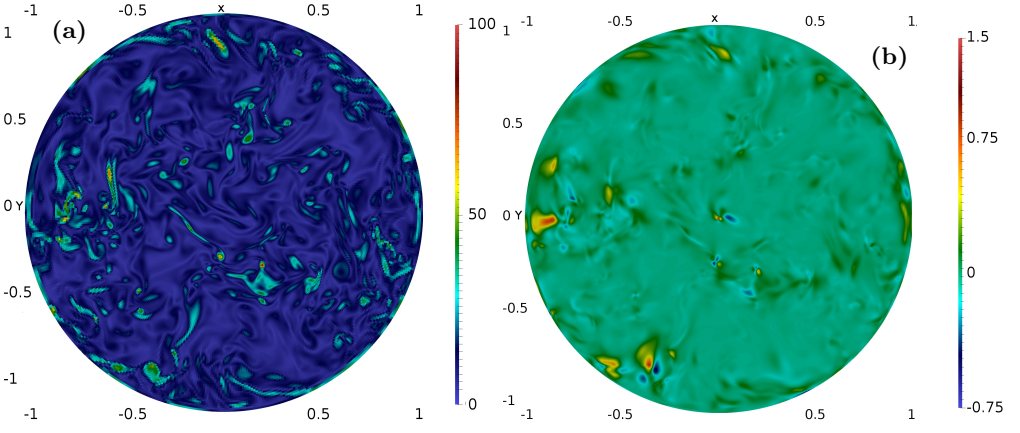

FIGURE 2. Visualization of the vorticity amplitude of ω (a) and $\mathscr{D}_\ell^{\mathrm{I}}$ (b) for $\ell = 8\eta$ on a plane containing the center perpendicular to the cylinder's axis from the DNS of table 1.

between $\omega/\langle\omega\rangle$ and $\mathscr{D}_\ell^{\mathrm{I}}/\epsilon$. We have investigated the spatial distribution of the events corresponding to this tail in an instantaneous snapshot. It is displayed in figure 5. We see that these events are organized into coherent structures, with three favoured locations: i) at the blade forefront, in the impeller region, where each blade strongly pushes the flow; ii) at the outer edge of the disk supporting the impeller; iii) in two blobs that are lying near the cylinder edge, and just above or just below the middle shear layer. While the first two types of events can be associated to local gradient sources due to the impellers that are difficult to measure experimentally, the last category corresponds to the location of the strong vortices of the shear layer. The latter are known to be present in the von Kármán geometry (Ravelet et al. 2008) and they are the locus of strong energy transfers (Marie & Daviaud 2004; Kuzzay et al. 2015). This explains why such events have both strong vorticity, and strong local energy transfer. The absence of strong correlated events in the middle of the tank may explain why joint PDF $\mathbb{P}\big(\frac{\mathscr{D}_\ell^{\mathrm{I}}}{\epsilon}, \frac{\omega}{\langle\omega\rangle}\big)$ based on experiment

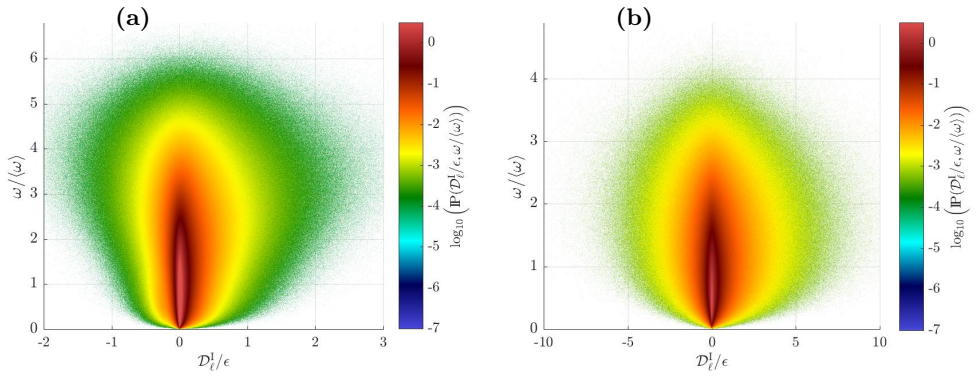

FIGURE 3. Joint-PDF of $\mathbb{P}\left(\frac{\mathscr{D}^{\mathrm{I}}_\ell}{\epsilon}, \frac{\omega}{\langle\omega\rangle}\right)$ for different scales from experimental measurements in table 1 computed over several uncorrelated snapshots. Here ω refers to the norm of the vorticity, and $\mathscr{D}^{\mathrm{I}}_\ell$ is the energy transfer. **a**) T-4: $\ell = 3.2\eta$ (3 10^4 snapshots) **b**) T-2: $\ell = 17.9\eta$ (1.02 10^4 snapshots). White color corresponds to lack of events in the data-set.

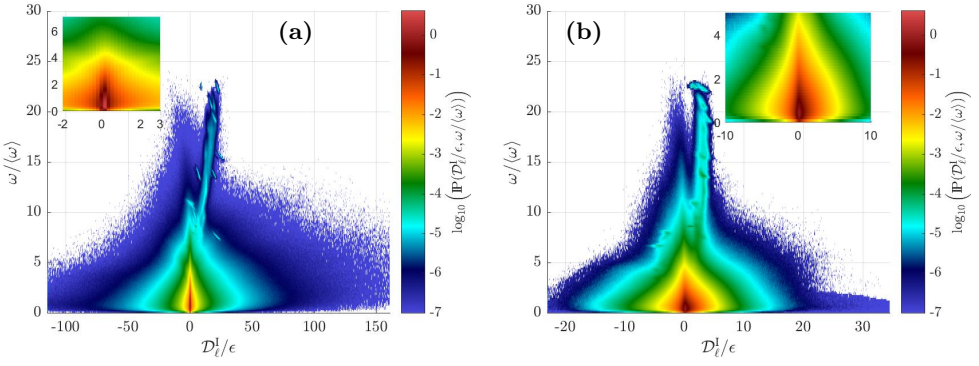

FIGURE 4. Joint-PDF of $\mathbb{P}\left(\frac{\mathscr{D}^{\mathrm{I}}_\ell}{\epsilon}, \frac{\omega}{\langle\omega\rangle}\right)$ for different scales from the DNS in table 1 computed over 21 uncorrelated snapshots. ω refers to the norm of the vorticity, and $\mathscr{D}^{\mathrm{I}}_\ell$ is the energy transfer. A zoom on the central region is presented on each panel to compare with figure 3. **a**) $\ell = 1.06\eta$ **b**) $\ell = 26.5\eta$. White color corresponds to lack of events in the data-set.

T-4 do not exhibit the tail, since the corresponding data were only taken in a small cube at the center of the tank.

Using the joint PDF, we have computed the conditional average $\mathbb{E}\left(\frac{\mathscr{D}^{\mathrm{I}}_\ell}{\epsilon}|\frac{\omega}{\langle\omega\rangle}\right)$ as the average of $\frac{\mathscr{D}^{\mathrm{I}}_\ell}{\epsilon}$ over the points where $\frac{\omega}{\langle\omega\rangle}$ is fixed. It is plotted on figure 6 as a function of $\left(\frac{\omega}{\langle\omega\rangle}\right)^2$ both in the numerical and experimental cases. For $\ell \sim \eta$, the conditional average $\mathbb{E}\left(\frac{\mathscr{D}^{\mathrm{I}}_\ell}{\epsilon}|\frac{\omega}{\langle\omega\rangle}\right)$ increases almost linearly with $\left(\frac{\omega}{\langle\omega\rangle}\right)^2$. For large $\ell \gg \eta$ the conditional averages seem to reach a plateau where the local energy transfers do not depend anymore on the vorticity, meaning that there is no correlation at large scales. This feature is more pronounced on the DNS than in the experiment. This shows that local energy transfers and vorticity are only correlated at small scales.

In order to investigate the link between the energy transfers and velocity increments, the joint PDF of $\mathscr{D}^{\mathrm{I}}_\ell$ with the full (δW_ℓ) and anti-symmetric ($\delta\Omega_\ell$) components of the velocity increments are plotted in figures 7 and 8. It appears that positive values of $\mathscr{D}^{\mathrm{I}}_\ell$ are promoted for both quantities. In the inertial range, it seems that the large $\mathscr{D}^{\mathrm{I}}_\ell$ are

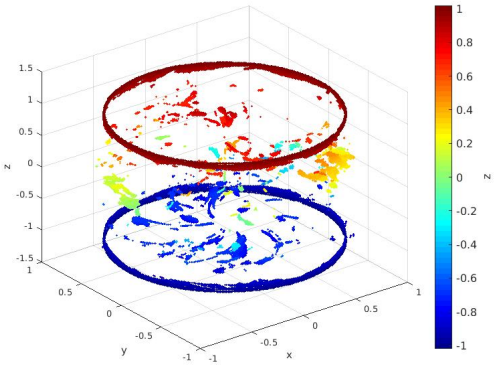

FIGURE 5. Positions of DNS points in the tail of figure 4-b where $\mathscr{D}^{\mathrm{I}}_{\ell} > \epsilon$ and $\omega > 5\langle\omega\rangle$ for $\ell = 26.5\eta$. The colors correspond to the z values of the points, indicating that most of them are close to the impellers ($0.7 < |z| < 1.02$), or at the tank mid-height. This plots shows positions for one single snapshot.

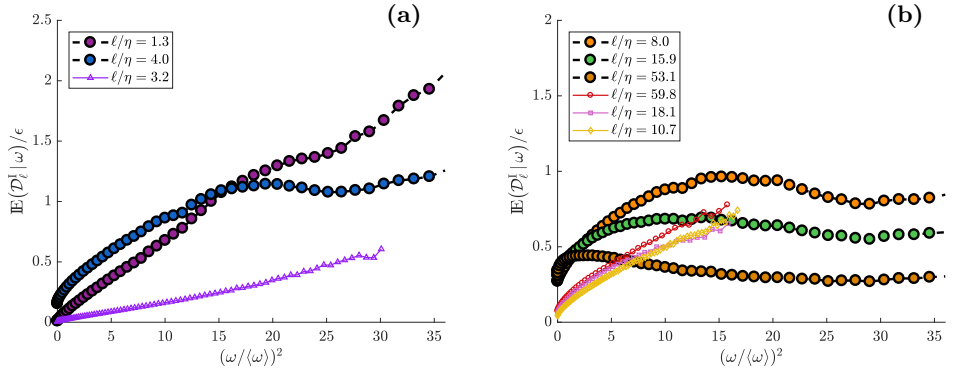

FIGURE 6. Conditional average $\mathbb{E}\left(\mathscr{D}^{\mathrm{I}}_{\ell}|\omega\right)/\epsilon$ as a function of $(\omega/\langle\omega\rangle)^2$for different scales ℓ. They are computed from joint PDFs as the ones in figures 3 and 4 from datasets of the DNS and cases T-1 to T-4 in table 1. Symbols are coded according to table 1.

more correlated with strong events of $\delta\Omega_{\ell}$ than with δW_{ℓ}, since the PDF of $\left(\mathscr{D}^{\mathrm{I}}_{\ell}, \delta\Omega_{\ell}\right)$ is more tilted to the right hand side, and most of the positive energy transfers are associated with increments of the order of several times the mean value.

4.3. *Local energy transfers*

We now focus on the scale behaviour of the statistical average of the local energy transfer $\mathscr{D}^{\mathrm{I}}_{\ell}$, and the local energy dissipation $\mathscr{D}^{\nu}_{\ell}$. The comparison between numerical and experimental data is performed in figure 9-a. For each experimental dataset, a filtering process is applied to the data giving a range of accessible ℓ scaling from Δx to approximately $10\Delta x$ depending on the size of the PIV grid. Combining all datasets with accessible R_{λ}, ϵ and η allows to cover a wide range of scales in terms of $\frac{\ell}{\eta}$. They all behave according to the K41 phenomenology (Dubrulle 2019): the local energy transfer is much lower than the local energy dissipation for $\ell/\eta < 10$ and saturates beyond to a constant value, while the local energy dissipation decreases from the dissipative range to the large scales following a $\ell^{-4/3}$ law. The agreement between experimental data and numerical data is very good for $\mathscr{D}^{\nu}_{\ell}$, but poor for $\mathscr{D}^{\mathrm{I}}_{\ell}$. We assign such mismatch to

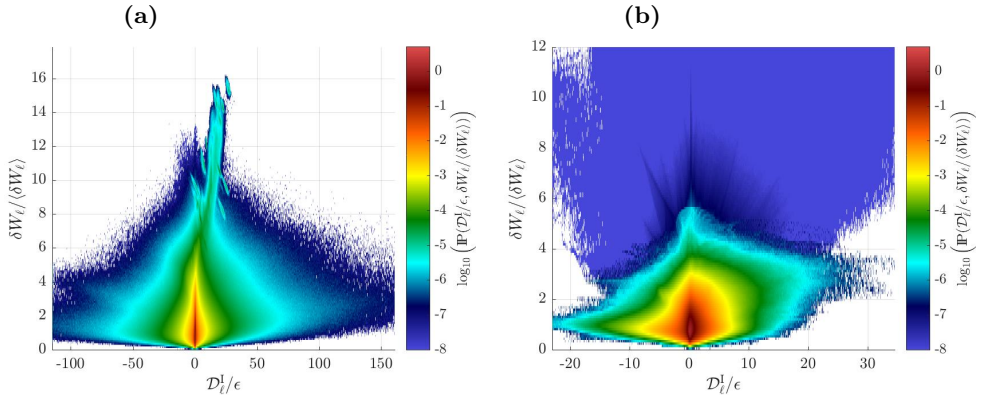

FIGURE 7. Joint-pdf of $\mathbb{P}\left(\frac{\mathscr{D}^{\mathrm{I}}_\ell}{\epsilon}, \frac{\delta W_\ell}{\langle\delta W_\ell\rangle}\right)$ for different scales from the DNS in table 1 computed over 21 uncorrelated snapshots. **a**) $\ell = 1.06\eta$ **b**) $\ell = 26.5\eta$. White color corresponds to lack of events in the data-set.

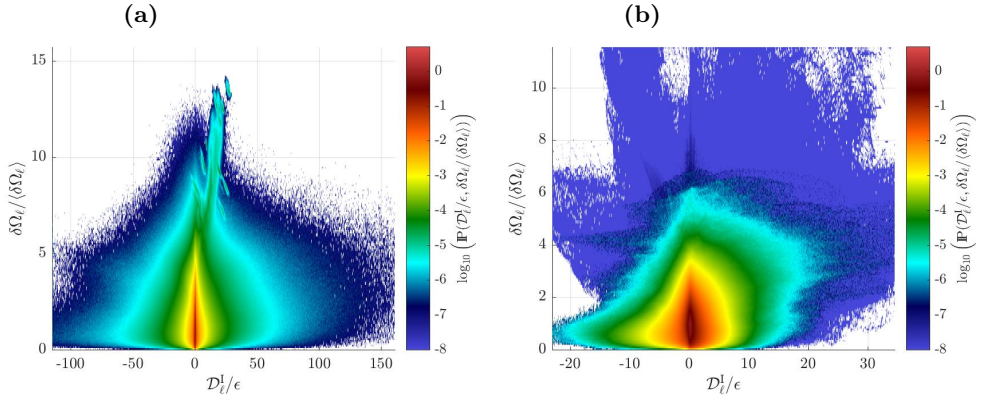

FIGURE 8. Joint-pdf of $\mathbb{P}\left(\frac{\mathscr{D}^{\mathrm{I}}_\ell}{\epsilon}, \frac{\delta\Omega\ell}{\langle\delta\Omega\ell\rangle}\right)$ for different scales from the DNS in table 1 computed over 21 uncorrelated snapshots. **a**) $\ell = 1.06\eta$ **b**) $\ell = 26.5\eta$. White color corresponds to lack of events in the data-set.

convergence effects: indeed, even if our statistical samples are quite large, the presence of very large events in the local transfer that can be both positive or negative renders the statistics very difficult to converge. Note that $\mathcal{D}^{\nu}_\ell$ is mainly positive, so that the plots in figure 9-a of $\langle\mathcal{D}^{\nu}_\ell\rangle$ and figure 9-b of $\langle|\mathcal{D}^{\nu}_\ell|\rangle$ are almost the same. These plots show that the agreement is excellent between experimental and DNS data. In contrast, $\mathcal{D}^{\mathrm{I}}_\ell$ takes extreme positive and negative values. We suspect that it is the reason why the statistics of $\langle\mathcal{D}^{\mathrm{I}}_\ell\rangle$ in figure 9-a are less well converged. To test this idea, we plot in figure 9-b $\langle|\mathcal{D}^{\mathrm{I}}_\ell|\rangle$ which shows that statistics are indeed improved. This issue is linked to the presence of rare events of extreme values of $\mathcal{D}^{\mathrm{I}}_\ell$, that is discussed in the appendix of Debue et al. (2018) for experimental points. A convergence study of the DNS statistics is presented in the appendix (figure 15). On the other hand, the local dissipation, that is always positive, does not suffer from such drawback. To check such hypothesis, we plot in figure 9-b the average of absolute value of $\mathscr{D}^{\mathrm{I}}_\ell$ and $\mathscr{D}^{\nu}_\ell$. Indeed, we see that the data are less scattered, and that data points corresponding to different experiments follow a clear trend. The numerical data is closer to the TPIV data than the SPIV data. This might be due to the fact that SPIV data are 2D-3C, meaning that some components of $\mathscr{D}^{\mathrm{I}}_\ell$ are missing. These plots show that the "inertial range" (location where $\mathscr{D}^{\mathrm{I}}_\ell$ is constant), extends from

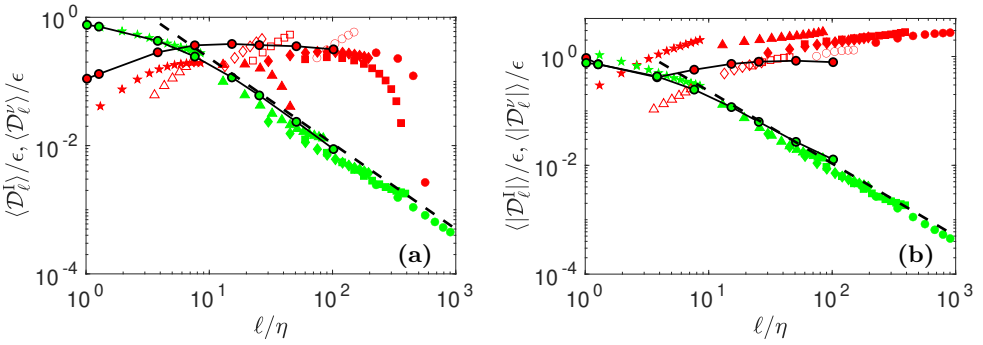

FIGURE 9. Scale variation of the non-dimensional the local energy transfer (red) and dissipation (green) for SPIV experiments A to E (filled symbol), TPIV experiments (open symbols) and the DNS (filled symbols with black line). Dotted lines correspond to $\ell^{-\frac{4}{3}}$. a) for $\mathscr{D}_\ell^{\mathrm{I}}$ and $\mathscr{D}_\ell^{\nu}$ non-dimensionalized by the total energy dissipation in the observational box; b) Same for absolute values. The symbols are coded according to table 1.

$\ell/\eta = 20$ to $\ell/\eta = 100$ for the numerical data. Such observation will be used to compute the scaling exponents in section 4.6.

4.4. *Structure functions*

Longitudinal and wavelet velocity structure functions, as well as non-dimensional moments of $\mathscr{D}_\ell^{\mathrm{I}}$, have been previously computed and discussed in Saw et al. (2018); Debue et al. (2018); Dubrulle (2019) from the experimental SPIV data sets A to E of table 1, with the drawback that the velocity field is only 2D-3C. Here, we repeat their computation with experimental and numerical 3D-3C data, with focus on the wavelet velocity structure functions that are more appropriate for our purpose, see Section 2.2. Figure 10-a shows the comparison of the compensated wavelet velocity structure functions $\tilde{S}_W(p) = \langle \delta W_\ell^p \rangle / \langle \delta W_\ell^3 \rangle^{p/3}$ of order 1 to 6 for numerical and experimental SPIV data. One sees that they are in good agreement for $p = 1$ to 4, and that the agreement deteriorates at large scales for higher p. This is probably due to a lack of convergence for the numerical data because of limited sampling. The same comparison has been done for the anti-symmetric wavelet velocity structure functions in figure 10-b, leading to similar conclusion.

Finally, we compare the compensated moments of the local energy transfer $\mathscr{D}_\ell^{\mathrm{I}}$ for numerical and experimental data in figure 11-a. There is good agreement between numerical data and experiments in the inertial range, but not in the dissipative range or at large scales.

4.5. *Test of log-universality*

In figure (11)-a, we compare structure functions of the local energy transfer using data at different Reynolds numbers (see table 1). In agreement with Kolmogorov self-similarity hypothesis, we can expect, and we indeed observe that they have a universal behaviour in the inertial range, but not outside. As first discussed by Frisch & Vergassola (1991) and Castaing et al. (1990), a more general log-universality property can be expected using the multi-fractal hypothesis, if one works with variables that are rescaled by a factor proportional to $\log(R_\lambda)$, where R_λ is the Taylor Reynolds number. In Geneste et al. (2019), we have indeed shown that such rescaling enables a better collapse of the velocity structure functions S_W, and linked such log-universality with extensivity of

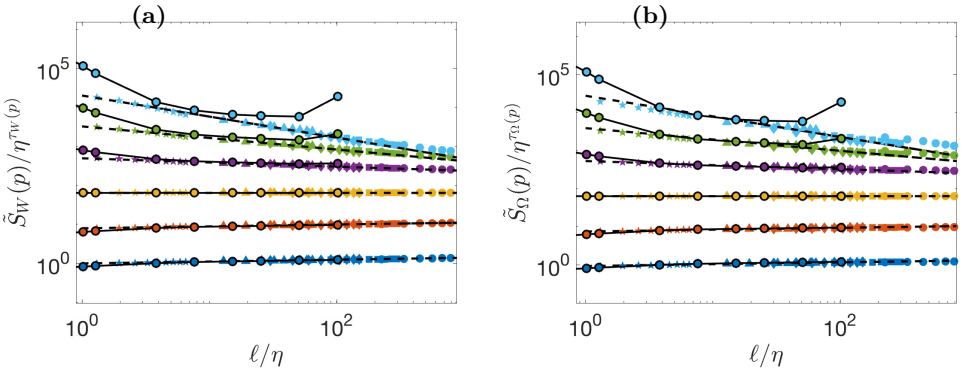

FIGURE 10. Scale variation of the normalized non-dimensional wavelet structure functions of order $p = 1$ to $p = 6$ for SPIV experiments A to E (filled symbol) and the DNS (filled symbols with black line) The structure functions have been shifted by arbitrary factors for clarity and are coded by color: $p = 1$: blue symbols; $p = 2$: orange symbols; $p = 3$: yellow symbols; $p = 4$: magenta symbols; $p = 5$: green symbols; $p = 6$: light blue symbols. a) Structure functions $\tilde{S}_W(p)$. b) Structure functions for the anti-symmetric component $\tilde{S}_\Omega(p)$. The dashed lines are power laws with exponents τ_W and τ_Ω shown in figure 13-a. The symbols are coded according to table 1.

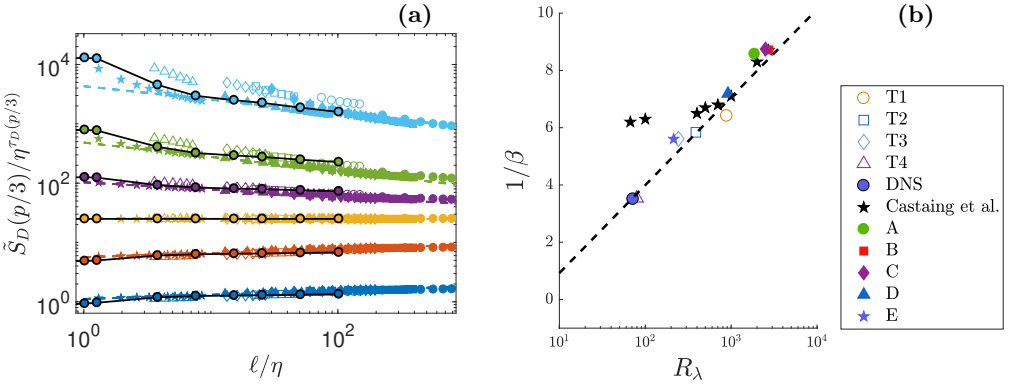

FIGURE 11. a) Scale variation of the compensated structure functions of the local energy transfer $\tilde{S}_D(p/3)$ of order $p = 1$ to 6 for SPIV experiments A to E (filled symbol), TPIV experiments (open symbols) and the DNS (filled symbols with black line). The structure functions have been shifted by arbitrary factors for clarity and are coded by color: $p = 1$: blue symbols; $p = 2$: orange symbols; $p = 3$: yellow symbols; $p = 4$: magenta symbols; $p = 5$: green symbols; $p = 6$: light blue symbols. The dashed lines are power laws with exponents τ_D shown in figure 13-a. The symbols are coded according to table 1. b) Parameter β given in eq. (4.1). Names are taken accordingly to table 1. The dotted line follows the equation $1/\beta = \frac{4}{3}\log(R_\lambda)$.

the large deviation function of the multi-fractal measure $\delta W_\ell^3/\langle \delta W_\ell^3 \rangle$. If the local refined similarity hypothesis (2.9) holds true, one can expect that the log-universality also applies to the measure $|\mathscr{D}_\ell^{\mathrm{I}}|/\langle |\mathscr{D}_\ell^{\mathrm{I}}| \rangle$, so that:

$$\beta(\mathrm{Re}) \left(\frac{\ln(\tilde{S}_D(p)/S_{0p})}{\ln(L_0/\eta)} \right) = F\left(p, \beta(\mathrm{Re}) \frac{\ln(\ell/\eta)}{\ln(L_0/\eta)} \right). \tag{4.1}$$

We take the DNS at $R_\lambda = 72$ as the reference case, and find, for both DNS and experiments, values of $\beta(Re)$ and S_{0p} that best collapse the curves. The corresponding collapses are provided in figure 12. The collapse is good for any value, except for the TPIV at the lowest Reynolds number, which does not collapse in the dissipative range.

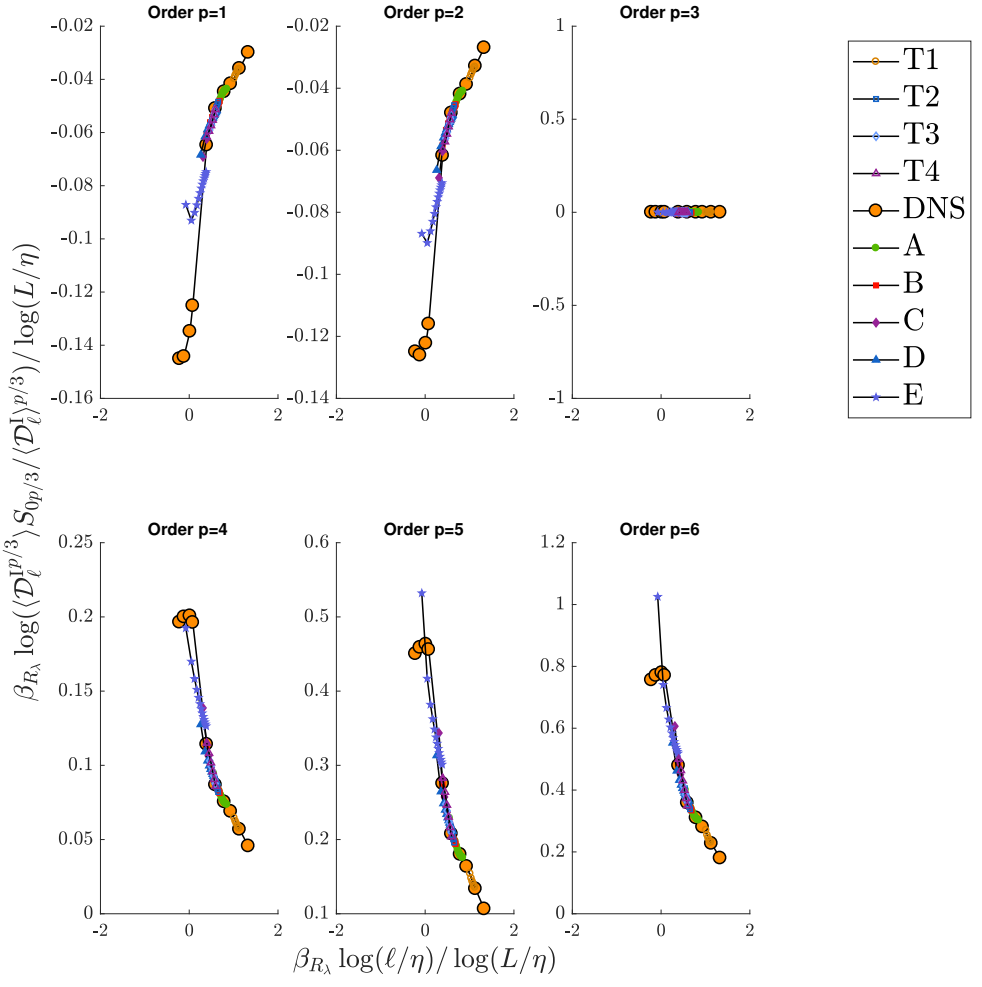

FIGURE 12. Computation of eq. (4.1) from order $p = 1$ to order $p = 6$. Collapse is made for all experiments presented in table 1, using DNS (orange circle) as the reference and the β parameter taken from figure 11-b

The collapsing curves display three different scaling regimes. At low ℓ/η, a saturation can only be seen on the DNS, which corresponds to the far viscous range, where the velocity field becomes regular, so that $\langle |\mathscr{D}_\ell^{\mathrm{I}}|^p \rangle \sim \ell^{2p}$ (Dubrulle 2019), and $S_D(p) \sim cte$. In the inertial range, we observe a scaling $S_D(p) \sim \ell^{\tau_D(p)}$ and in between, an intermediate range due to the random character of the dissipative scale, corresponding to the coexistence of regions of flow with different Hölder exponents, with areas where the flow has been relaminarized due to the action of viscosity (Geneste et al. 2019).

The values of $\beta(Re)$ are shown in figure 11-b. In agreement with previous results (Geneste et al. 2019), they collapse on a curve $\frac{1}{\beta} \sim \frac{1}{\beta_0} \log(R_\lambda)$, with $\beta_0 \sim \frac{3}{4}$ over the whole range of Reynolds number, and we do not observe the saturation of $1/\beta$ at low Reynolds numbers that is observed in the jet experiment of Castaing et al. (1993).

4.6. *Scaling Exponents and Multi-fractal spectrum*

Using the identification of the inertial range based on the local energy transfer (see Section 4.3), we compute from figures 10 and 11 the scaling exponents $\tau_W(p)$, $\tau_\Omega(p)$

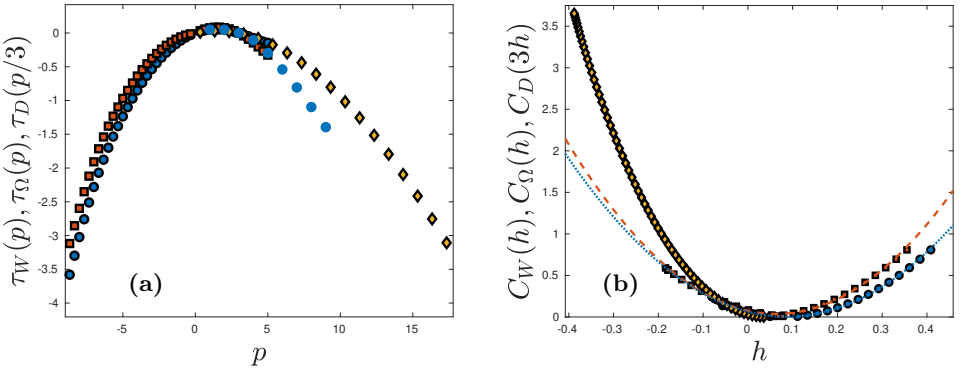

FIGURE 13. a) Scaling exponents as a function of order for DNS (filled symbols with black outside) and SPIV (filled symbol): τ_W: blue circle; τ_Ω: red square; τ_D: yellow diamond. (b) Corresponding multi-fractal spectrum $C(h)$ for the DNS scaling exponents. The spectrum has been obtained by taking the inverse Legendre transform of the scaling exponents $\tau(p)$ shown in figure 13-a. The dotted line curves are parabolic fit $C(h) = ah^2 + bh + c$ with $a = 8$ (resp. 9.5), $b = -1.4$ (resp. -1.2) and $c = 0.064$ (resp. 0.075) for C_W (resp C_Ω).

and $\tau_D(p/3)$ for the numerical data. They are shown in figure (13)-a. We see that $\tau_W(p)$ and $\tau_\Omega(p)$ overlap in the range $p \in [-5, 5]$, and overlap both with $\tau_D(p/3)$ in the range $p \in [0, 5]$, thereby validating the refined similarity hypothesis expressed by eq. (2.9) (Dubrulle 2019). These overlapping values computed from numerical data compare very well with the value $\tau_W(p)$ computed on the SPIV data by Debue et al. (2018); Dubrulle (2019). We checked that the values of $\tau_D(p/3)$ coincide with the values obtained using figure (12). We also completed our measurements by computing more positive and negative moments, so as to be able to better estimate the multi-fractal spectra $C_W(h)$, $C_\Omega(h)$ and $C_D(h)$ by Legendre transforms (see eq. (2.13)). The resulting spectra are shown in figure 13-b. The two spectra $C_W(h)$ and $C_\Omega(h)$ are parabolic, with a minimum shifted from 0 by about $\delta h = 0.08$. They are very close to each other for $h < 0$ but differ more markedly for $h > 0$, implying a different topology of regular regions. The value $C_W(h) = 3$ or $C_\Omega(h) = 3$ extrapolated from the parabolic fit results in $h_{\min} \approx -0.53$. Using the shift property (2.14) and the measurement of $\zeta_W(3) = 0.8$ (Dubrulle 2019), we can then estimate the most probable exponent for ζ_W and ζ_Ω as 0.35, very close to the Kolmogorov value 0.33. The minimum exponent for $C(h)$ is then $h_{\min} = -0.26$. Note that the multi-fractal spectrum of the local energy transfer $C_D(3h)$ deviates strongly from the parabolic fit of $C_W(h)$, and displays a milder intermittency, as it is more peaked around the most probable value. This is not caused by insufficient statistics as the values of $\tau_D(p/3)$ are not converged (see appendix) but could be caused by finite resolution (the finer scale is not small enough), meaning that we missed some very large energy transfers (Dubrulle 2019), or due to a genuine difference between intermittency at very small scales caused by vorticity and the local energy transfer. To try understanding further the origin of intermittency, we then attempt another approach, based on conditional statistics.

4.7. *Conditioned Scaling Exponents*

To understand further the origin of intermittency, it is natural to condition the structure functions to areas of different values of the local energy transfer. An earlier attempt in that direction has been done in Debue et al. (2018), for the SPIV data, with the limitation that the conditioning could only be done on the local energy transfer at

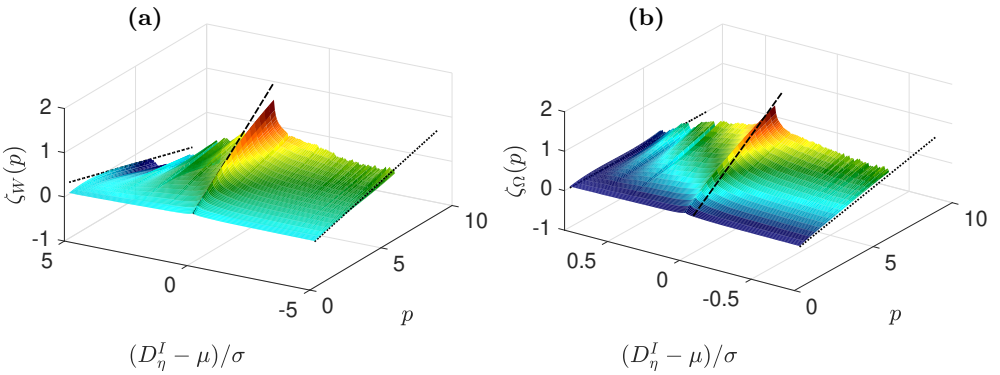

FIGURE 14. (a) Scaling exponent of the non-compensated wavelet structure functions S_W computed using the joint PDF of the centred and reduced value of $\mathscr{D}_\eta^{\mathrm{I}}$ and δW_ℓ at various scales ℓ, and then a fit in the inertial range. The dotted lines have a slope of -0.1 for large positive values of centred and reduced value of $\mathscr{D}_\eta^{\mathrm{I}}$, $1/3$ for small values of centred and reduced value of $\mathscr{D}_\eta^{\mathrm{I}}$, and 0.1 for large negative values of centred and reduced value of $\mathscr{D}_\eta^{\mathrm{I}}$. (b) Same as a), using the joint PDF of the centred and reduced value of $\mathscr{D}_\eta^{\mathrm{I}}$ and $\delta\Omega_\ell$. The dotted lines have a slope of 0 for large positive values of centred and reduced value of $\mathscr{D}_\eta^{\mathrm{I}}$, $1/3$ for small values of centred and reduced value of $\mathscr{D}_\eta^{\mathrm{I}}$, and 0.1 for large negative values of centred and reduced value of $\mathscr{D}_\eta^{\mathrm{I}}$.

the smallest available scale of the data set. Therefore, the conditioning was performed at the Kolmogorov scale only for the data set E. The conclusion of such conditioning was that the intermittency was higher for areas corresponding to a larger (in absolute value) local energy transfer.

Using the data from the DNS, we can improve the procedure, by conditioning the structure functions at all scales by the local energy transfer at the Kolmogorov scale $\mathscr{D}_\eta^{\mathrm{I}}$. Here, we enlarge the discussion by considering positive and negative values of the local energy transfer, as they may correspond to different dynamics. Because of the conditioning, we have less statistics so we have to restrict ourselves to smaller values of p than for unconditioned values. Once the structure functions have been conditioned, we can compute the corresponding conditioned scaling exponent by fitting power laws in the inertial range. The results for S_W are shown in figure 14-a, for p ranging from 0 to 6 and for centred reduced values of $\mathscr{D}_\eta^{\mathrm{I}}$ ranging from -5 to 5. One sees that for values $\mathscr{D}_\eta^{\mathrm{I}}$ close to the mean, the scaling exponents are positive, and close to the Kolmogorov value $p/3$. For large negative $\mathscr{D}_\eta^{\mathrm{I}}$, the scaling exponents are positive, but increase linearly with a small exponent $h_- \sim 0.1$. For large positive $\mathscr{D}_\eta^{\mathrm{I}}$, the scaling exponents decrease quasi linearly with a small exponent $h_+ \sim -0.1$. This shows that negative local energy transfers are less intermittent than positive local energy transfers. The corresponding values of h are close to 0, reminiscent of shock like structures. Exploring more singular structures closer to $h = -0.26$ (the minimum exponent of $C(h)$) would require a much larger number of statistics. We have repeated the analyses for the structure functions of the vortical part S_Ω in figure 14-b. We observe a similar trend for large negative and positive values of $\mathscr{D}_\eta^{\mathrm{I}}$, where we see that the scaling exponents are much more intermittent than for $\mathscr{D}_\eta^{\mathrm{I}}$ around its mean value. In both cases, the conditioned exponent displays linear trends with $h_- \sim 0.1$ and $h_+ \sim 0$, exponents that are close to their counterpart using S_W. Such a linear trend might be an indication that only one type of very singular structure is responsible for the scaling behaviour of S_W or S_Ω for large positive or negative local energy transfers.

5. Discussion

We have conducted an extensive study of the scaling properties of small scale turbulence using both numerical and experimental data of a flow in the von Kármán geometry. Our investigations validate both Kraichnan intuition, and Batchelor early observation: areas of strong vorticity are correlated to areas of strong local energy transfer; both are highly intermittent, and responsible for deviations of the structure functions from the Kolmogorov 1941 simple mono-fractal picture. Such findings are not surprising given the already known link between intermittency and dissipation (Kolmogorov 1962), from the one hand, and dissipation and enstrophy and dissipation and local energy transfer (Dubrulle 2019) on the other hand. These results show once more the necessity to deal with very small scales of turbulence when it comes to the modelling of realistic velocity fluctuations, a problematic issue when considering very high Reynolds number flows, in which the ratio of the integral to the dissipative scale goes like $\mathrm{Re}^{3/4}$.

On the other hand, the correlation we find between vorticity and local energy transfer is not perfect: in the joint PDF, we observe in figure 4 a stretched diamond shape for values of ω that are not too high, demonstrating that large value of local energy transfers are correlated to medium values of ω, while areas of large ω are independent of local energy transfer. This is an indication that the location of local maxima of energy transfer is shifted with respect to the location of the local maxima of vorticity, a fact already observed in our experiment (Debue 2019; Debue et al. 2020) and in numerical simulations (Nguyen et al. 2019). This points out the complex dynamics of the small scale structures of turbulence, and calls for further investigation, to determine the role of local energy transfer in the formation of high vorticity zone, or the reverse.

Quite interestingly, we have nevertheless gathered several indications that in the von Kármán flow the most intermittent structures might have an interesting simple structure: first, the linear trend between the conditional average of $|\mathscr{D}_\ell^{\mathrm{I}}|$ versus ω^2 for scales small enough; second, the linear trend of the conditional scaling exponent of S_W or S_Ω, observed for high negative or positive values of the local energy transfer in our numerical data in figure 14 ; finally, the linear tails observed in the joint PDF between the vorticity and the local energy transfer in our numerical data (figure 4), that corresponds partly to strong vortices of the shear layer. This location corresponds obviously to areas where the shear, hence the dissipation and the fluctuations, are maximum. In Marie & Daviaud (2004), it was indeed found that most of the angular momentum transfer occurs in such zone via correlated azimuthal and vertical velocity fluctuations. Such location (near the cylinder boundary, at the mid-height) is also the location where Luo & Hou (2014) detected a potential singularity in an Euler axisymmetric flow with a geometry similar to the shear layer geometry. The blowing up solution was furthermore shown to develop a self-similar structure near the point of the singularity, as the singularity time is approached.

Whether the vortices of the von Kármán shear layer we evidenced in figure 5 correspond to self-similar quasi-singularities of the Euler equations, that could dominate the scaling properties at large orders, is an interesting issue that is worth investigating further with time correlated snapshots. Indeed, they could act as the counter-part of the self-similar blowing solution of inviscid Burgers equation or shell models that have been found recently to control the intermittency in such systems (Mailybaev 2015). To explore such interesting connection, we need to follow in space and time the dynamics of such structures, which is both an experimental and numerical challenge, for different reasons (noise issue in the first case, numerical burden in the second). Such studies are nevertheless underway.

Finally, it would also be interesting to perform a similar analysis of the link between area of high energy transfers and large vorticities in other geometries, so as to explore whether our findings are due to the peculiar geometry of the von Kármán flow (with a shear layer and a stagnation point in the middle) or are linked with universal features of turbulent flows.

Acknowledgement This work has been funded by the ANR, project EXPLOIT, grant agreement no. ANR-16-CE06-0006-01, and project ECOUTURB grant agreement no. ANR-16-CE30-0016. This work has also been founded by the Funding agency LabEx PALM Investissement d'Avenir under the grant number ANR-10-LABX-0039-PALM. Access to the HPC resources were provided by IDRIS (institut du développement et des ressources en informatique scientifique) under the allocation 2019-0254 made by GENCI (Grand Equipement National de Calcul Intensif).

Declaration of Interests. The authors report no conflict of interest.

REFERENCES

Batchelor, G. K. & Townsend, A. A. 1949 The nature of turbulent motion at large wave-numbers. *Proceedings of the Royal Society of London. Series A. Mathematical and Physical Sciences* **199** (1057), 238–255, arXiv: https://royalsocietypublishing.org/doi/pdf/10.1098/rspa.1949.0136.

Cappanera, L, Debue, P, Faller, H, Kuzzay, D, Saw, E-W., Nore, C, Guermond, J-L, Daviaud, F, Wiertel-Gasquet, C & Dubrulle, B 2020 Turbulence in realistic geometries with moving boundaries: when simulations meet experiments. *Under revision in Computers & Fluids* , arXiv: https://hal.archives-ouvertes.fr/hal-02928403.

Castaing, B., Gagne, Y. & Hopfinger, E.J. 1990 Velocity probability density functions of high Reynolds number turbulence. *Physica D: Nonlinear Phenomena* **46** (2), 177 – 200.

Castaing, B, Gagne, Y & Marchand, M 1993 Log-similarity for turbulent flows? *Physica D: Nonlinear Phenomena* **68** (3), 387 – 400.

Chainais, P, Abry, P & Pinton, J-F 1999 Intermittency and coherent structures in a swirling flow: A wavelet analysis of joint pressure and velocity measurements. *Physics of Fluids* **11** (11), 3524–3539.

Debue, Paul 2019 Experimental approach to the problem of the Navier-Stokes singularities. Thesis, Université Paris-Saclay.

Debue, P., Shukla, V., Kuzzay, D., Faranda, D., Saw, E.-W., Daviaud, F. & Dubrulle, B. 2018 Dissipation, intermittency, and singularities in incompressible turbulent flows. *Phys. Rev. E* **97**, 053101.

Debue, P, Valori, V, Cuvier, C, Daviaud, F, Foucaut, J-M, Laval, J-P, Wiertel-Gasquet, C, Padilla, V & Dubrulle, B 2020 3D analysis of precursors to non-viscous dissipation in an experimental turbulent flow. *submitted to J. Fluid Mech.* .

Dubrulle, Bérengère 1994 Intermittency in fully developed turbulence: Log-poisson statistics and generalized scale covariance. *Phys. Rev. Lett.* **73**, 959–962.

Dubrulle, B 2019 Beyond Kolmogorov cascades. *Journal of Fluid Mechanics* **867**, P1.

Farge, Marie 1992 Wavelet transforms and their applications to turbulence. *Annual Review of Fluid Mechanics* **24** (1), 395–458, arXiv: https://doi.org/10.1146/annurev.fl.24.010192.002143.

Frisch, U. & Parisi, G. 1985 On the singularity structure of fully developed turbulence. In Turbulence and Predictability in Geophysical Fluid Dynamics and ClimateDynamics (ed. M. Gil, R. Benzi & G. Parisi), pp. 84–88. Amsterdam, North-Holland: Elsevier.

Frisch, U & Vergassola, M 1991 A prediction of the multifractal model: the intermediate dissipation range. *Europhysics Letters (EPL)* **14** (5), 439–444.

Geneste, D, Faller, H, Nguyen, F, Shukla, V, Laval, J-P, Daviaud, F, Saw, E-W & Dubrulle, B 2019 About universality and thermodynamics of turbulence. *Entropy* **21** (3).

Kestener, P. & Arneodo, A. 2004 Generalizing the wavelet-based multifractal formalism to

vector-valued random fields: application to turbulent velocity and vorticity 3D numerical data. *Phys. Rev. Lett* **93** (4).

Kolmogorov, A. 1941 The Local Structure of Turbulence in Incompressible Viscous Fluid for Very Large Reynolds' Numbers. *Akademiia Nauk SSSR Doklady* **30**, 301–305.

Kolmogorov, A. N. 1962 A refinement of previous hypotheses concerning the local structure of turbulence in a viscous incompressible fluid at high Reynolds number. *Journal of Fluid Mechanics* **13** (1), 8285.

Kraichnan, R. H. 1975 Remarks on turbulence theory. *Advances in Mathematics* **16** (3), 305 – 331.

Kuzzay, D, Faranda, D & Dubrulle, B 2015 Global vs local energy dissipation: The energy cycle of the turbulent von Kármán flow. *Physics of Fluids* **27**, 075105.

Luo, G. & Hou, T. Y. 2014 Potentially singular solutions of the 3d axisymmetric euler equations. *Proceedings of the National Academy of Sciences* **111** (36), 1296812973.

Mailybaev, A-A 2015 Continuous representation for shell models of turbulence. *Nonlinearity* **28** (7), 2497–2514.

Marie, L. & Daviaud, F. 2004 Experimental measurement of the scale-by-scale momentum transport budget in a turbulent shear flow. *Physics of Fluids* **16** (2), 457–461.

Meneveau, Charles 1991 Analysis of turbulence in the orthonormal wavelet representation. *Journal of Fluid Mechanics* **232**, 469520.

Moffatt, H.K. 2002 G.K. Batchelor and the homogenization of turbulence. *Annual Review of Fluid Mechanics* **34** (1), 19–35, arXiv: https://doi.org/10.1146/annurev.fluid.34.081701.134821.

Moisy, F. & Jiménez, J. 2004 Geometry and clustering of intense structures in isotropic turbulence. *Journal of Fluid Mechanics* **513**, 111133.

Muzy, J. F., Bacry, E. & Arneodo, A. 1991 Wavelets and multifractal formalism for singular signals: Application to turbulence data. *Phys. Rev. Lett.* **67** (25), 3515.

Nguyen, F., Laval, J-P., Kestener, P., Cheskidov, A., Shvydkoy, R. & Dubrulle, B. 2019 Local estimates of Holder exponents in turbulent vector fields. *Physical Review E* **99**.

Nore, C., Castanon Quiroz, D., Cappanera, L. & Guermond, J.-L. 2018 Numerical simulation of the von Krmn sodium dynamo experiment. *Journal of Fluid Mechanics* **854**, 164195.

Ostovan, Yasar, Cuvier, Christophe, Debue, Paul, Valori, Valentina, Cheminet, Adam, Foucaut, Jean-Marc, Laval, Jean-Philippe, Wiertel-Gasquet, Cécile, Vincent, Padilla, Dubrulle, Bérengère & others 2019 4D particle tracking velocimetry measurements in a von Kármán turbulence experiment. *ISPIV conference* .

Ouellette, Nicholas T, Xu, Haitao, Bourgoin, Mickal & Bodenschatz, Eberhard 2006 Small-scale anisotropy in lagrangian turbulence. *New Journal of Physics* **8** (6), 102–102.

Paret, J & Tabeling, P 1998 Intermittency in the two-dimensional inverse cascade of energy: Experimental observations. *Physics of Fluids* **10** (12), 3126–3136, arXiv: https://doi.org/10.1063/1.869840.

Ravelet, F, Chiffaudel, A & Daviaud, F 2008 Supercritical transition to turbulence in an inertially driven von Kármán closed flow. *Journal of Fluid Mechanics* **601**, 339–364.

Saw, E.-W., Debue, P., Kuzzay, D., Daviaud, F. & Dubrulle, B. 2018 On the universality of anomalous scaling exponents of structure functions in turbulent flows. *J. Fluid Mech.* **837**, 657–669.

Saw, E. W., Kuzzay, D., Faranda, D., Guittonneau, A., Daviaud, F., Wiertel-Gasquet, C., Padilla, V. & Dubrulle, B. 2016 Experimental characterization of extreme events of inertial dissipation in a turbulent swirling flow. *Nature Communications* **7** (12466).

Schneider, Kai & Vasilyev, Oleg V. 2010 Wavelet methods in computational fluid dynamics. *Annual Review of Fluid Mechanics* **42** (1), 473–503, arXiv: https://doi.org/10.1146/annurev-fluid-121108-145637.

Vincent, A. & Meneguzzi, M. 1994 The dynamics of vorticity tubes in homogeneous turbulence. *Journal of Fluid Mechanics* **258**, 245254.

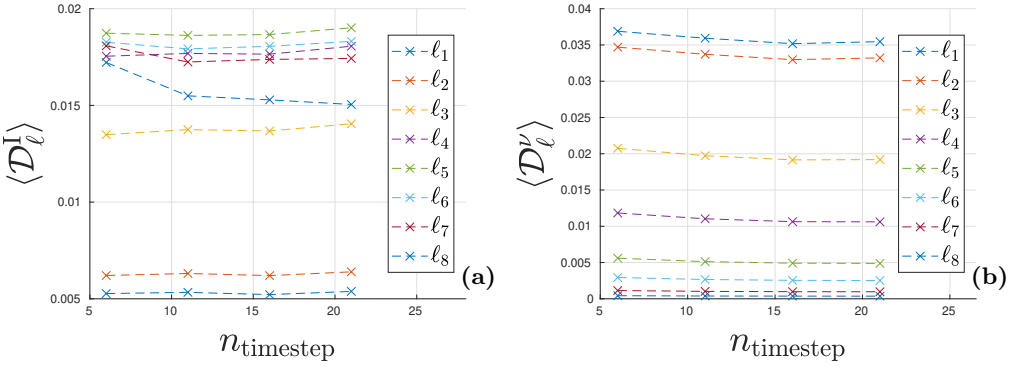

FIGURE 15. Convergence of mean DNS quantities for the 8 scales ($\ell_1 < \ell_2 < ... < \ell_8$) presented in figure 9-a computed on 6, 11, 16 or 21 snapshots. **a**) $\langle \mathscr{D}_\ell^{\mathrm{I}} \rangle$ **b**) $\langle \mathscr{D}_\ell^{\nu} \rangle$

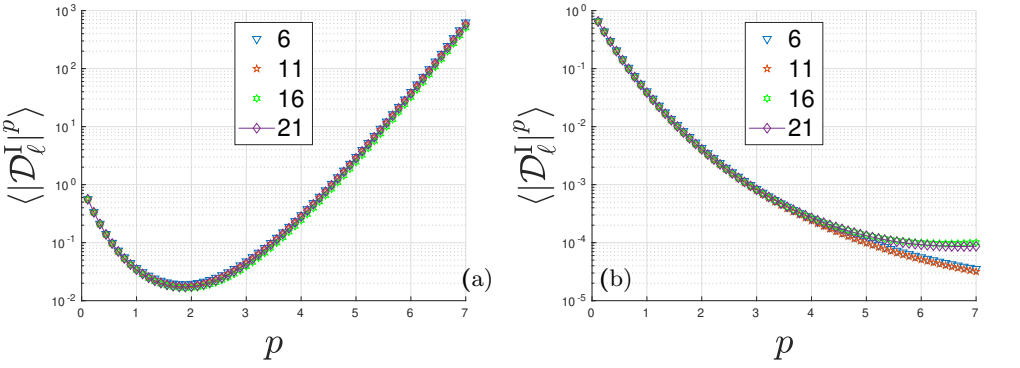

FIGURE 16. Moments of $|\mathscr{D}_\ell^{\mathrm{I}}|$ computed on 6, 11, 16 or 21 snapshots. **a**) $\ell = 1.06\eta$ **b**) $\ell = 26.5\eta$

Appendix

DNS statistical convergence study

DNS data cover 21 uncorrelated snapshots of 3 10^8 grid points. To evaluate the convergence of the DNS data, we present here the empirical moments and mean values computed on an increasing number of snapshots. First of all, the averages $\langle \mathscr{D}_\ell^{\mathrm{I}} \rangle$ and $\langle \mathscr{D}_\ell^{\nu} \rangle$ used in figure 9-a are converged as figure 15 shows. We can then focus on the moments of the statistical quantities. In the viscous range, for $\ell = 1.06\eta$ (figures 16-a, 17-a and 18-a), the convergence is good for all p since the statistics on 16 or 21 snapshots agree, and the 21-snapshots results lay between the 11-snapshots and 16-snapshots ones. In the inertial range, for $\ell = 26.5\eta$ (figures 16-b, 17-b and 18-b), the moments are converged for the same reasons up to $p = 5$, but not totally converged for $p \geqslant 5$ since the results do not coincide and decrease monotonically for velocity increments δW_ℓ and $\delta \Omega_\ell$ as the dataset-size increases. Since the moments are used to compute the exponents $\tau(p)$, figure 13 only shows velocity and energy transfers intermittency exponents up to $p = 5$ for DNS.

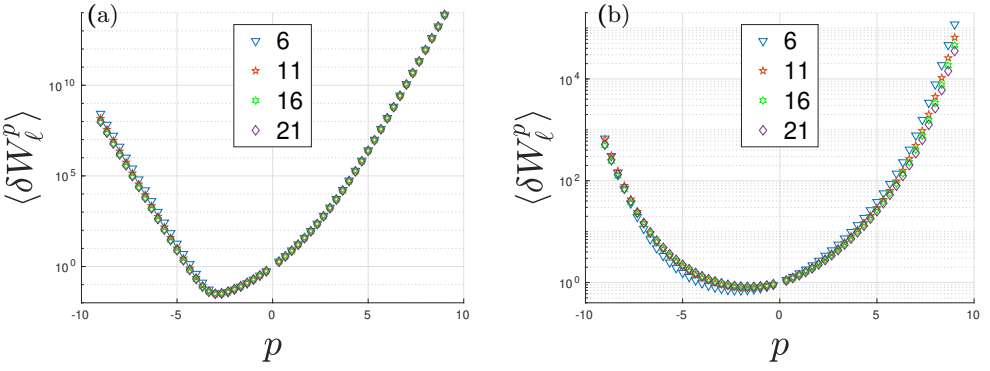

FIGURE 17. Moments of δW_ℓ computed on 6, 11, 16 or 21 snapshots. **a**) $\ell = 1.06\eta$ **b**) $\ell = 26.5\eta$

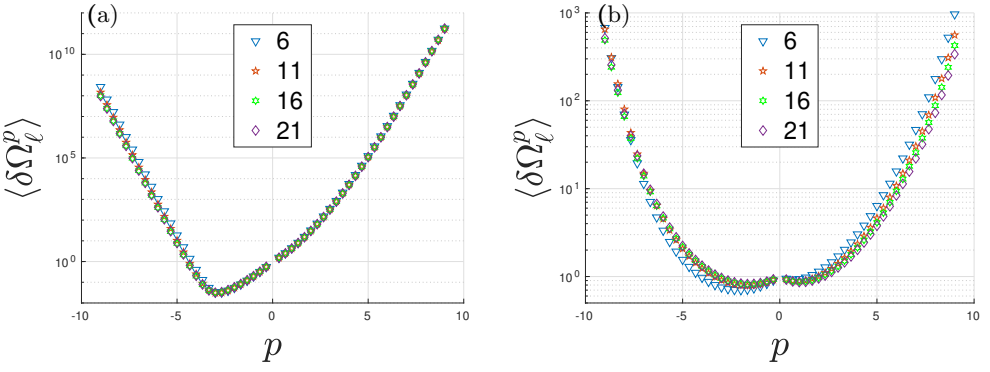

FIGURE 18. Moments of $\delta \Omega_\ell$ computed on 6, 11, 16 or 21 snapshots. **a**) $\ell = 1.06\eta$ **b**) $\ell = 26.5\eta$